Supporting information

Suspended silicon waveguide platform with subwavelength grating metamaterial cladding for long-wave infrared sensing applications

*Weixin Liu, Yiming Ma, Yuhua Chang, Bowei Dong, Jingxuan Wei, Zhihao Ren, and Chengkuo Lee**

Department of Electrical and Computer Engineering, National University of Singapore, Singapore, 117583, Singapore

Center for Intelligent Sensors and MEMS, National University of Singapore, Singapore, 117608, Singapore

These authors contribute equally: Weixin Liu, Yiming Ma.

E-mail: elelc@nus.edu.sg

S1. Calculation of the evanescent field ratio and the effective sensing length

The external confinement factor Γ_{clad}, representing a measure of interaction of the guided mode with the cladding, is quantified via perturbation theory:

$$\Gamma_{clad} = \frac{d_{n_{eff}}}{d_{n_{clad}}} = \frac{n_g}{n_{clad}} \frac{\iiint_{clad} \varepsilon \left|\vec{E}\right|^2 dxdydz}{\iiint_{-\infty}^{\infty} \varepsilon \left|\vec{E}\right|^2 dxdydz}$$

Where n_g is the group index, n_{clad} is the cladding refractive index, ε(x, y, z) is the permittivity, and E(x, y, z) is the electric field. In this work, n_g is preliminarily calculated at around 3.83 for the fabricated structure. In 3-D FDTD simulation, a cuboid monitor with a = 1 μm, b = 7.5 μm, c = 10 μm is placed to extract spatial distribution of E(x, y, z), as shown in Figure S1. The mesh resolution is 100 pixel/μm along the x-direction, 100 pixel/μm along the y-direction, and 75 pixel/μm along the z-direction. Based on the simulation, the Γ_{clad} is calculated as 24.3%.

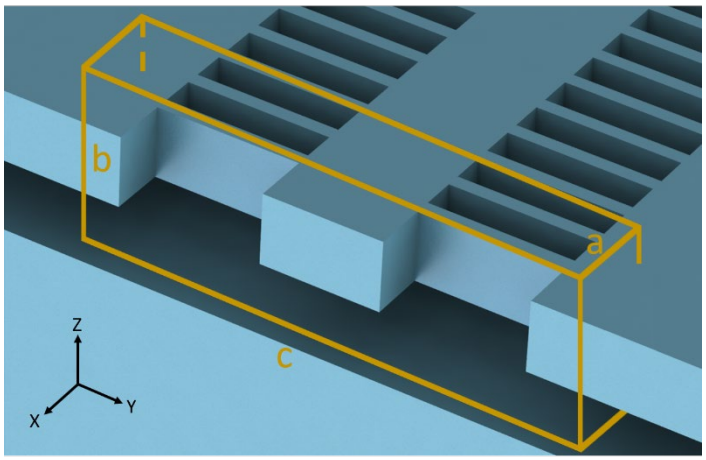

Figure S1. Schematic illustration of the 3D FDTD simulation.

The waveguide sensor follows Beer's law:

$$T = I_{\text{toluene}}/I_{ref} = \exp(-\alpha \Gamma_{clad} LC)$$

where T is the transmittance, I_{toluene} is the detector signal under the toluene-N_2 mixture. I_{ref} is the signal under pure N_2, α is the absorption coefficient of toluene vapor. L is the physical waveguide length, which in our case, is 28.4 mm. C is the concentration of the analyte. Therefore, the effective sensing length is calculated as $L_{\text{eff}} = \Gamma_{clad} L$= 6.9 mm.

S2. Summary of MIR grating couplers

Table S1. Summary of MIR grating couplers

Platform	Central wavelength (μm)	Maximum coupling efficiency (dB)	1-dB bandwidth (nm)	3-dB bandwidth (nm)	Ref
Suspended Si (from SOI)	**6.63**	**-7**	**170**	**304**	**This work**
Ge-on-Si	6.95	N/A	N/A	500	[S1]
Ge-on-Si	5.2	-5	N/A	100	[S2]
Ge-on-SOI	5.2	-4	N/A	180	
Suspended Si (from SOI)	2.75	-6.07	N/A	N/A	[S3]
SOI	2.1	-3.8	N/A	90	[S4]
SOI	3.75	-7.37	152	263.5	[S5]
	3.68	-6.48	N/A	199	
Si-on-Sapphire	3.43	-5.38	N/A	N/A	[S6]
SOS	2.75	-4.87	N/A	N/A	[S7]
Suspended Ge	2.37	-11	58	N/A	[S8]
Ge-on-Si	3.8	-11	70	N/A	[S9]
Ge-on-Si	3.8	-16.5	70	N/A	[S10]

In Table S1, we summarize the operating wavelengths and performances of reported MIR grating couplers. It is worth noting that few of the reported grating couplers operate in the LWIR range. Our work contributes to the supplementary of functional blocks in this regime based on the SOI platform. The proposed grating coupler has a maximum coupling efficiency of -7 dB and 3-dB bandwidth of 304 nm, centered at 6.63 μm. As Table S1 depicted, the performance of our grating coupler is comparable to that of others in the MIR, achieving a balance between the coupling efficiency and the bandwidth.

S3. Summary of MIR waveguide platforms

Table S2. Summary of MIR waveguide platforms

Platform	Wavelength (μm)	Propagation loss (dB/cm)	Bending loss (dB/bend)	Demonstrated building blocks					Ref
				GC	Y junctions	DC	Ring resonator	MMI	
Suspended Si	**6.4 – 6.8**	**4.3 ± 0.39**	**0.06**	**√**	**√**	**√**			**This work**
Suspended Si	7.67	3.1	0.08						[S11]
Ge-on-Si	6.7 – 7.45	< 5	N/A	√					[S1]
Ge-on-Si	6.85 – 11.25	< 10	N/A						[S12]
Ge-on-Si	7.5 – 8.5	2.5	N/A	√				√	[S13]
Graded SiGe	8.5	< 3	N/A						[S14]
Suspended Ge	7.67	2.65	N/A						[S15]
Ge-Sb-Ge	7.7	2.5	N/A						[S16]
Si-on-CaF_2	5.1 – 5.3	3.8	< 0.1				√		[S17]
Si-on-Sapphire	5.4 – 5.6	4.0 ± 0.7	N/A				√		[S18]
Diamond	5 – 7	~ 5.5	N/A						[S19]
Suspended Si	4.24	3 ± 1	N/A						[S20]
SOI	3.88	3	0.07			√			[S21]
Si-on-Nitride	3.39	5.1	N/A						[S22]
Ge-on-Nitride	3.73	7.86	N/A						[S23]
Si-on-Porous-Si	3.39	3.9	0.006						[S24]
AlN-on-Insulator	3.65 – 3.9	8.2	0.2			√	√	√	[S25]

(GC: grating coupler; DC: directional coupler; MMI: multi-mode interferometer)

We also summarize the reported MIR waveguide platforms in Table S2. Compared with previous works, our platform shows comparable propagation loss and bending loss but not recorded high. While the simulation results suggest propagation loss of only 1.5 dB/cm, the extra loss is possibly attributed to the surface roughness produced in our etching process. Suspended Si waveguides developed in Ref. S11 show a propagation loss of 3.1 dB/cm, in which the material loss of Si contributes ~2.1 dB/cm. Therefore, by further optimizing the fabrication process of our platform, we believe a lower propagation loss could be achieved.

Apart from the loss characterization, the development of various functional building blocks is essential for the realization of integrated photonic systems. As presented in Table S2, despite the demonstrations in other platforms or at lower wavelengths, the development of LWIR functional building blocks in the suspended Si platform, which origins from the most mature SOI, is still lacking. Motivated by this, we demonstrated LWIR suspended Si grating couplers, Y-junctions, and directional couplers for the first time with good performance, aiming for the system integration of LWIR gas sensors. Besides, the comprehensive study of SWG cladding on sensing enhancement also guarantees the achieved low LoD in our experiment.

S4. Influence of the flow rate

In our experiment, the flow rate of the gas is fast enough to deliver toluene to the vicinity of the waveguide. To verified this, we have measured the response times and recovery times under different flow rates of 4 L/min and 8 L/min, respectively, as shown in Figure S2. Compared with the results under 2 L/min flow rate as shown in Figure 6C and D, no significant change in either response time or recovery time is observed in the experiment, indicating the response time and recovery time are mainly limited by the nanophotonic platform.

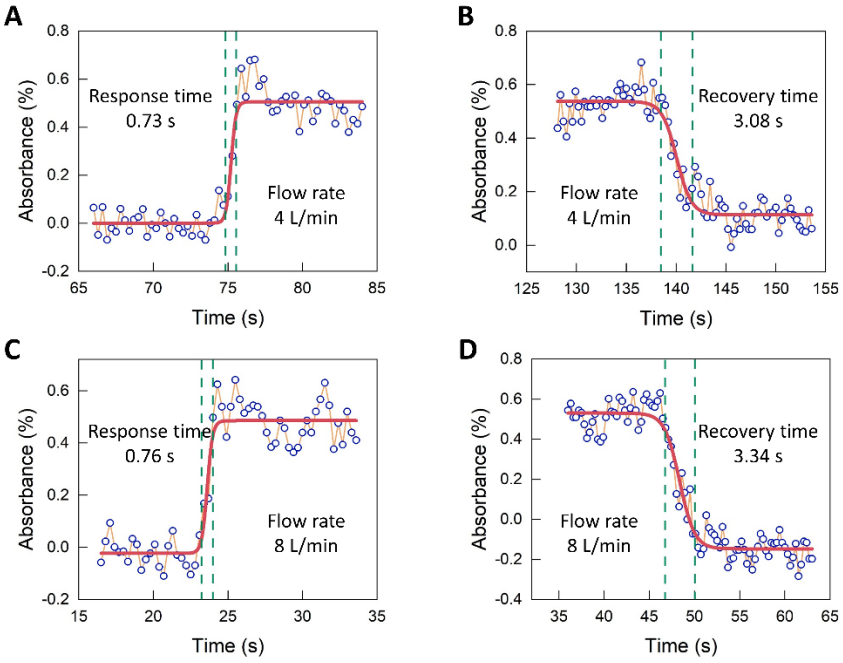

Figure S2. (A) Response time and (B) recovery time under the flow rate of 4L/min; (C) response time and (D) recovery time under the flow rate of 8 L/min.

S5. Analysis of the off-chip noises

In our experiment, the off-chip noise floor mainly consists of MCT detector noise and laser power fluctuation. Among these, the detector noise almost keeps constant regardless of the signal power, while the laser power fluctuation is proportional to the laser intensity. We have characterized the relationship between noise level and signal intensity further to identify noise components, as plotted in Figure S3. The slope of the linear fitting suggests that the laser power fluctuation occupies ~0.038% of the signal, while the intercept mainly represents the detector noise of ~12.5 μV. Therefore, for our typical measurement with signal power between 5×10^4 μV and 1×10^6 μV, the noise attributes to the laser fluctuation is around 19 μV – 380 μV. This means most of the measured noise attributes to the laser fluctuation at a higher signal intensity. Therefore, by employing a low-noise light source, we can further reduce the LoD of our platform to several ppm.

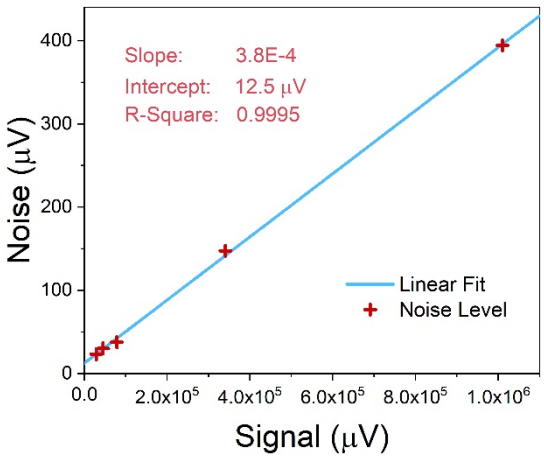

Figure S3. The noise level as a function of the signal measured in our system. The slope of the linear fitting suggests a laser power fluctuation of 0.038% of the signal, while the intercept suggests a constant photodetector noise of ~12.5 μV.

References

[S1] Benéitez NT, Baumgartner B, Missinne J, et al. Mid-IR sensing platform for trace analysis in aqueous solutions based on a germanium-on-silicon waveguide chip with a mesoporous silica coating for analyte enrichment. Opt Express 2020;28:27013-27.

[S2] Radosavljevic S, Kuyken B, Roelkens G. Efficient 5.2 μm wavelength fiber-to-chip grating couplers for the Ge-on-Si and Ge-on-SOI mid-infrared waveguide platform. Opt Express 2017;25:19034-42.

[S3] Cheng Z, Chen X, Wong CY, et al. Focusing subwavelength grating coupler for mid-infrared suspended membrane waveguide. Opt Lett 2012;37:1217-9.

[S4] Hattasan N, Kuyken B, Leo F, et al. High-Efficiency SOI Fiber-to-Chip Grating Couplers and Low-Loss Waveguides for the Short-Wave Infrared. IEEE Photonics Technol Lett 2012;24:1536-8.

[S5] Chen N, Dong B, Luo X, et al. Efficient and broadband subwavelength grating coupler for 3.7 μm mid-infrared silicon photonics integration. Opt Express 2018;26:26242-56.

[S6] Zou Y, Subbaraman H, Chakravarty S, et al. Grating-coupled silicon-on-sapphire integrated slot waveguides operating at mid-infrared wavelengths. Opt Lett 2014;39:3070-3.

[S7] Cheng Z, Chen X, Wong CY, et al. Mid-infrared grating couplers for silicon-on-sapphire waveguides. IEEE Photonics J 2012;4:104-13.

[S8] Kang J, Cheng Z, Zhou W, et al. Focusing subwavelength grating coupler for mid-infrared suspended membrane germanium waveguides. Opt Lett 2017;42:2094-7.

[S9] Alonso-Ramos C, Nedeljkovic M, Benedikovic D, et al. Germanium-on-silicon mid-infrared grating couplers with low-reflectivity inverse taper excitation. Opt Lett 2016;41:4324-7.

[S10] Nedeljkovic M, Soler Penadés J, Mitchell CJ, et al. Surface grating coupled low loss Ge-on-Si rib waveguides and multimode interferometers. Photonics Technol Lett IEEE 2015;27:1040-3.

[S11] Penadés JS, Sánchez-Postigo A, Nedeljkovic M, et al. Suspended silicon waveguides for long-wave infrared wavelengths. Opt Lett 2018;43:795-8.

[S12] Kozak DA, Stievater TH, Mahon R, et al. Germanium-on-Silicon Waveguides at Wavelengths from 6.85 to 11.25 microns. IEEE J Sel Top Quantum Electron 2018;24:8200804.

[S13] Nedeljkovic M, Penades JS, Mittal V, et al. Germanium-on-silicon waveguides operating at mid-infrared wavelengths up to 8.5 μm. Opt Express 2017;25:27431-41.

[S14] J.M.Ramirez, Q L, V.Vakarin, et al. Graded SiGe waveguides with broadband low-loss propagation in the mid-infrared. Opt Express 2018;26:870-7.

[S15] Osman A, Nedeljkovic M, Soler Penades J, et al. Suspended low-loss

germanium waveguides for the long-wave infrared. Opt Lett 2018;43:5997-6000.

[S16] Gutierrez-Arroyo A, Baudet E, Bodiou L, et al. Optical characterization at 7.7 μm of an integrated platform based on chalcogenide waveguides for sensing applications in the mid-infrared. Opt Express 2016;24:23109-17.

[S17] Chen Y, Lin H, Hu J, et al. Heterogeneously integrated silicon photonics for the mid-infrared and spectroscopic sensing. ACS Nano 2014;8:6955-61.

[S18] Spott A, Liu Y, Baehr-Jones T, et al. Silicon waveguides and ring resonators at 5.5 μm. Appl Phys Lett 2010;97:213501.

[S19] Haas J, Catalán EV, Piron P, et al. Polycrystalline Diamond Thin-Film Waveguides for Mid-Infrared Evanescent Field Sensors. ACS Omega 2018;3:6190-8.

[S20] Ottonello-Briano F, Errando-Herranz C, Rödjegård H, et al. Carbon dioxide absorption spectroscopy with a mid-infrared silicon photonic waveguide. Opt Lett 2020;45:109-12.

[S21] Dong B, Guo X, Ho CP, et al. Silicon-on-Insulator Waveguide Devices for Broadband Mid-Infrared Photonics. IEEE Photonics J 2017;9:4501410.

[S22] Khan S, Chiles J, Ma J, et al. Silicon-on-nitride waveguides for mid- and near-infrared integrated photonics. Appl Phys Lett 2013;102:121104.

[S23] Li W, Anantha P, Lee KH, et al. Spiral Waveguides on Germanium-on-Silicon Nitride Platform for Mid-IR Sensing Applications. IEEE Photonics J 2018;10:2201107.

[S24] Mashanovich GZ, Milošević MM, Nedeljkovic M, et al. Low loss silicon waveguides for the mid-infrared. Opt Express 2011;19:7112-9.

[S25] Dong B, Luo X, Zhu S, et al. Thermal annealing study of the mid-infrared aluminum nitride on insulator (AlNOI) photonics platform. Opt Express 2019;22:19815-26.